COMPUTER AND COMPUTATIONAL SCIENCES

Seed Money Fund

Cardiopulmonary Resuscitation Using Optimal Control

E. Jung,[1,2*] S. M. Lenhart,[1] and V. A. Protopopescu[1]
[1]*Computer Science and Mathematics Division*
[2]*Konkuk University, Seoul, South Korea*

Optimal control (OC) techniques are applied for the first time to a model of standard cardiopulmonary resuscitation (CPR). Pattern of control of the pressure on the chest is implemented on a validated blood circulation model consisting of a system of seven difference equations. The externally applied chest pressure acting as the "control" is the nonhomogeneous forcing term in this system. The OC approach seeks to maximize the blood flow, as measured by the pressure differences between the thoracic aorta and the right heart and superior vena cava.

Introduction

Each year, more than 250,000 people die in the USA from cardiac arrest. Despite widespread use of CPR, the survival of patients revived from cardiac arrest remains poor. The rate of survival for CPR performed outside the hospital is 3%. For patients who have CPR in the hospital, the rate of survival is 10–15%. The practical technique of CPR has changed little since the 1960s. The technique of OC proposes a strategy for improving resuscitation rates using a validated circulation model developed by Babbs.[1]

Technical Approach

We apply OC techniques for the first time to a CPR model. The idea is to develop a new CPR strategy to improve resuscitation rates. The chosen CPR model consists of seven difference equations for the hemodynamics of adult human circulation. For the OC application, the circulation model is extended to include the control functions as discrete inputs. As a control, we choose the pattern of the pressure applied on the chest. The controls at the current time step and the previous time step enter the model in the calculation of pressures at the next time step. This type of input control is unusual and requires an innovative adaptation of the discrete version of Pontryagin's Maximum Principle.[2,3] To make the chest pressure profiles medically reasonable, we assumed that the admissible controls are zero at the beginning and end of the time interval.

In Babbs' model,[1] heart and blood vessels are represented as resistance-capacitive networks, pressures in the chest and vascular compartments as voltages, blood flow as electric current, and cardiac and venous valves as diodes (electrical devices that permit flow in only one direction). The following pressure variables are used: pressures in abdominal aorta, inferior vena aorta, carotid, jugular, thoracic aorta, right heart and superior vena cava, and thoracic pump. There is one difference equation for the time evolution of each pressure variable. Valves are incorporated into the equations for the pressures in jugular, thoracic aorta, right heart and superior vena cava, and the thoracic pump.

The OC seeks to maximize the blood flow as measured by the pressure differences between the thoracic aorta and the right heart and superior vena cava. The goal is to maximize this pressure difference summed over the time steps subject to a stabilizing control size minimization.[1] The flow is measured in systemic perfusion pressure (SPP), a measure of the blood flow between the thoracic aorta and the right heart and superior vena cava. The "control to pressure" solution map and the "control to the goal" map are differentiated to characterize the optimal control. Existence, uniqueness, and explicit characterization of the OC were completed for this control problem. The OC is completely and explicitly characterized in terms of the solutions of the circulation model and the solution of an adjoint model. Uniqueness of the OC can also be shown under the assumptions that the time step size is small enough. For this discrete CPR model, the "natural" time step in this discrete CPR model depends on the other coefficients in the system. Whenever warranted, uniqueness is obtained by proving the uniqueness of the solution of the optimality system, obtained by coupling the original circulation system, the adjoint system, and the control characterization. Thus when

*This work was conducted in collaboration with Eunok Jung of Konkuk University, South Korea, who was an ORNL employee at the time of the initial work on this project. C. F. Babbs from Purdue University (consultant M.D. on this project) was involved in the setup and analysis of the OC problem.

the optimal control is numerically calculated through solving the optimality system, the uniqueness guarantees that we find the unique OC.

The numerical implementation of this control solution involves an iterative method with a forward sweep of the circulation model followed by a backward sweep of the adjoint model with a control characterization update afterwards. Since the circulation model has initial data and the adjoint system has data at the final time, the coupled system cannot be solved forward together. The iterative method starts with a guess for the control values, and then the control is updated after each forward sweep and backward sweep. The forward and backward sweeps are repeated until convergence of the iterates is achieved. Since we are using difference equations, the sweeps are "time stepping" through the interval. The state and adjoint equations give the next values from the previous values and control values from the last two steps. The resulting numerical code was run for a range of parameters which are reasonable for this CPR model. The "optimal" chest pressure profiles and the corresponding SPP were calculated on each run.

Results and Accomplishments

The OC procedure applied to Babbs' discrete CPR system resulted in an explicit characterization of the OC. The OC gives the chest pressure profile to be followed in the CPR process. Our OC chest pressure profile results in improvement over the standard CPR procedure used on this model.[1] The improvement is measured in SPP. In Fig. 1, we show a typical chest pressure example profile, "optimal control," for a certain set of parameters, which is appropriate for the standard heart model. The time scale

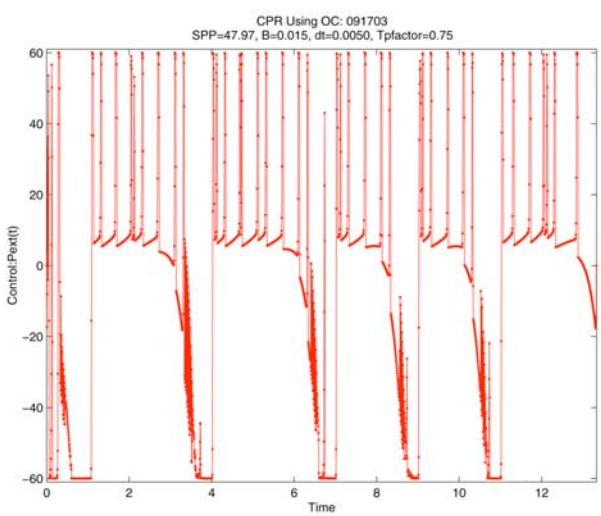

Fig. 1. Graph of the "optimal" chest pressure profile is given over a time scale in seconds. The term dt *is the size of the time step. The coefficient B is the stabilizing factor and "Tp factor" is the strength of the cardiac pump. The SPP is the systemic perfusion pressure (mmHg).*

is in seconds. The terms *dt* gives the size of the time step. The coefficient *B* is the stabilizing factor, and *Tp* factor is the strength of the cardiac pump. The SPP for this example is much higher than the SPP from the standard CPR technique as seen in Babbs' work;[1] we see about 20% improvement in SPP in our various examples. The fluctuation seen in this profile is typical of many of the examples we ran and indicates that rapid changes in pressure levels can make a significant improvement in SPP. This profile can be considered as a type of CPR with active compression and decompression (ACD) of the chest. The SPP for our example compares favorably with the SPP calculated from the standard ACD procedure.[1]

While OC of discrete difference equations has been used for many physical models,[4] applying these control techniques to a CPR or heart model has not been done before. From a technical standpoint, the control entering into the system at two moments of time (current and immediate past time steps) and giving input to the pressure system at the next time introduces a novel feature and a non-trivial difficulty that has been addressed and solved here.

This improved CPR strategy can be implemented either by an emergency helper or by a portable pressure device, which can achieve the optimal chest pressure profile, as indicated by the OC. The device could be further optimized by using more detailed circulation models based on partial differential equations and even customized to account for various age, sex, and weight groups within the general population. Extensions to nonstandard CPR techniques can also be treated with this OC technique. This type of portable device should interest medical equipment firms as well as the Army, and we expect to submit external proposals to continue this type of work.

We have submitted a Report of Invention[5] documenting the novel idea of applying OC techniques for the first time to a model of CPR. In that report, we note the novelty and relevance of the transition from differential equations to difference equations for this application and focus on the implementation of the improved strategy on a portable CPR device. Finally, as a part this project, E. Jung and C. F. Babbs submitted a paper on "valveless pumping."[6] Medical evidence shows that valveless pumping may play an important role in CPR.

Summary and Conclusions

Based on the results of this research, an increase of 20% in blood flow (quantified by SPP) is to be expected as a result of applying optimized CPR strategies. This may represent the difference between life and death for many people who undergo cardiac arrest. Moreover the technique can be easily implemented using portable devices.

References

[1]C. F. Babbs, "CPR Techniques that Combine Chest and Abdominal Compression and Decompression: Hemodynamic Insights from a Spreadsheet Model," *Circulation* **100**, 2146–2152 (1999).

[2]L. S. Pontryagin, V. G. Boltyanskii, R. V. Gamkrelidze, and E. F. Mischchenko, *The Mathematical Theory of Optimal Processes,* Wiley , New York, 1962.

[3]F-T Fan and C-S Wang, *The Discrete Maximum Principle: A Study of Multistage Systems Optimization,* Wiley, New York, 1964.

[4]S. P. Sethi and G. L. Thompson, *Optimal Control Theory, Applications to Management Science and Economics,* Kluwer, Boston, 2nd edition, 2000.

[5]S. Lenhart, V. Protopopescu, and E. Jung, *Optimal Control of CPR Procedure*, Report of Invention, Oak Ridge National Laboratory, October 2003.

[6]C. F. Babbs and E. Jung, "Valveless Pumping: the Reflected Wave Hypothesis," submitted to *American Journal of Physics*.

Automated Image Analysis for Functional Genomics

J. R. Price,[1] Y. Liu,[2] D. Aykac,[1] K. Chourey,[2] and S. S. Gleason[1]
[1]*Engineering, Science, and Technology Division*
[2]*Life Sciences Division*

The primary goals of this project were (1) to construct a database of mitotic spindle imagery from wild-type and knockout (mutant) mouse cells and (2) to develop proof-of-concept, automated image analysis tools to characterize and compare the observed structures. The mitotic spindle is a crucial structure in cell-cycle progression, serving as the machinery for chromosome segregation. Furthermore, its tubulin-based structure is the target of many anti-cancer drugs. In this project, we collected fluorescent confocal microscopy images of mitotic spindles from wild-type, mutant, and drug-treated fixed cells. Quantitative image-based features and software to compute these features were developed. The software was then applied to the imagery data set, and the acquired sets of quantitative features were compared statistically. The results demonstrate that the spindle structure can indeed be characterized by the features computed via automated image analysis and, furthermore, that these features can vary statistically between the different cell types studied. These results imply that the proposed methodology may prove significantly beneficial in the search for new anti-cancer drug targets and in determining the roles of various proteins in cell-cycle progression, spindle checkpoint, and/or chromosome segregation.

Introduction

Data related to functional genomics research is often captured in image form by a variety of instruments such as the confocal microscope, the atomic force microscope, and/or the deconvolution microscope. Currently, much of the analysis of this data is performed manually—a well-trained person examines the image and attempts to make qualitative observations concerning the contents. In order to conduct statistically meaningful experiments, it is necessary that many, many images be produced and analyzed quantitatively. It is, however, prohibitively time-consuming for a human to manually analyze a large number of images and virtually impossible to do so quantitatively. To advance functional genomics understanding, automated image analysis will be required in a variety of experimental endeavors.

Previously, Yie Liu (co-principal investigator) found that VPARP (a protein complex) interacts with alpha, beta, and gamma tubulins in vivo (unpublished data). The interaction with the spindle and the specific roles of VPARP, however, are poorly understood. It has also been reported[1] that a tumor suppressor gene known as p53 is a passenger of the centrosome and that the absence of p53 could lead to abnormal centrosome amplification. As alpha and beta tubulins are core components of the microtubules and the mitotic spindle, and since the centrosome plays such a crucial role in the spindle formation and function, the aim of this project was to determine if quantifiable differences between wild-type, VPARP-knockout, and p53-knockout spindles could be detected and quantified. Furthermore, the image processing tools developed to analyze the images from these experiments can be used for similar analyses of other spindle-associated proteins which may prove to be potential targets for future cancer treatment strategies.

Technical Approach

In this project, five different cell types were established for study. These cell types, along with the corresponding shorthand names we will use for them in the remainder of this report, were as follows:

1. Primary wild-type (WT),
2. Primary VPARP-knockout (VPARP-KO),
3. p53-knockout (p53-KO),
4. p53-KO, treated with Taxol for 24 hours at 0.01 uM concentration (p53-KO-TaxLo),
5. p53-KO, treated with Taxol for 24 hours at 0.1 uM concentration (p53-KO-TaxHi).

These cells were fixed and then probed with fluorescent-labeled, anti-tubulin antibodies that attach to the spindles of metaphase cells. The spindles were then imaged via confocal microscopy. A three-dimensional (3D) stack of images was acquired for each spindle, where each image represents one "slice" of the spindle volume. Each element in such a 3D array will be referred to as a voxel, and the value of the voxel represents the fluorescence intensity and, hence, the amount of tubulin, at the

corresponding location. Forty different spindles were imaged, which included eight different spindles for each of the five cell types in the list above. One example of a spindle image is shown in Fig. 1. Note that, for visualization purposes, all layers in Fig. 1 have been summed in the z-direction to make a single two-dimensional (2D) image from the three-dimensional (3D) stack. Brighter areas indicate regions of higher tubulin concentration.

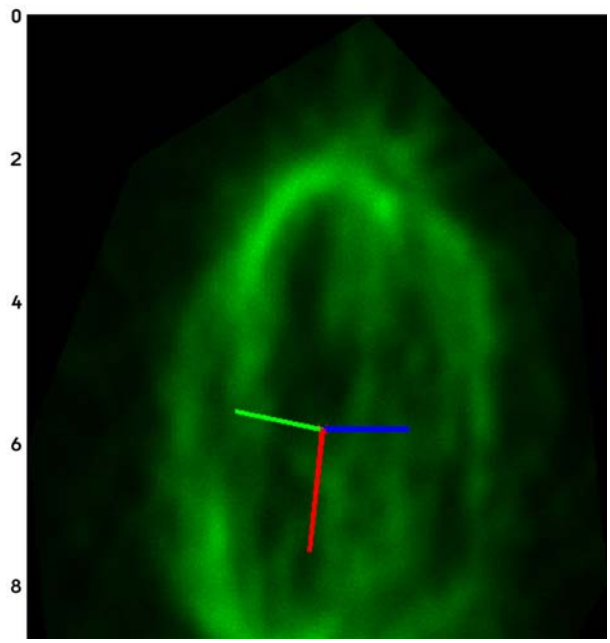

Fig. 1. Two-dimensional rendering of 3D spindle stack. The blue, green, and red lines indicate the first, second, and third principal axes, respectively. Units on both axes are in microns.

Each of the image stacks was then processed to produce a set of 49 descriptive features. The first eight features are independent of the spindle shape or geometry and depend only upon the voxel values. The remaining 40 features are morphology based and are computed with respect to an intrinsic coordinate system computed for each spindle. This intrinsic coordinate system has its origin at the spindle center of mass and axes aligned with the principal axes of inertia.[2] The center of mass and principal axes of inertia (and other mass-based features) are found by treating each voxel as a point mass, with mass equal to the voxel value, at the voxel location in the volume. Principal axes of inertia (projected onto the 2D viewing plane) are shown in the example spindle in Fig. 1. Below are brief descriptions of the 49 computed features.

1. Spindle mean. Average voxel value for the entire 3D stack.
2. Spindle standard deviation. Standard deviation of all voxel values in the stack.
3. Histogram skewness. Third central moment divided by the cube of the standard deviation. Gives a measure of the symmetry of the curve.
4. Histogram kurtosis. Fourth central moment divided by the fourth power of the standard deviation Gives a measure of how peaked the curve is.

5–8. Principal component coefficients of the histogram. We performed principal component analysis[3] on the 256-point histograms from the 40 spindle stacks. The coefficients of the histograms projected onto the first four principal components are kept for comparison.

9–12. Percentiles of mass projected onto first principal axis. These numbers are simply the intervals, in microns, along first principal axis which enclose 25%, 50%, 75%, and 95% of the total spindle mass.

13–16. Principal component coefficients of mass projected onto first principal axis. We project the spindle mass onto the first principal axis. Each point of the resulting curve, an example of which can be seen in see Fig. 2(a), represents the fraction of total spindle mass in the interval about that point. We use 200 intervals over the range of –10 to +10 μm about the center of mass.

17. Skewness of mass projected onto first principal axis.
18. Kurtosis of mass projected onto first principal axis.

19–22. Percentiles of mass projected onto second principal axis.

23–26. Principal component coefficients of mass projected onto second principal axis. An example curve of the mass projected on the second principal axis is shown in Fig. 2(b).

27. Skewness of mass projected onto second principal axis.
28. Kurtosis of mass projected onto second principal axis.

29–32. Percentiles of mass projected onto third principal axis.

33–36. Principal component coefficients of mass projected onto third principal axis. An example curve of the mass projected onto the third principal axis is shown in Fig. 2(c). Note the bimodal nature of this curve. This is due to the fact that the third principal axis—which is the axis about which the spindle has lowest moment of inertia—lies along the pole-to-pole axis of the spindle. The two peaks are related to the increased tubulin concentration at the spindle poles.

37. Kurtosis of mass projected onto third principal axis.

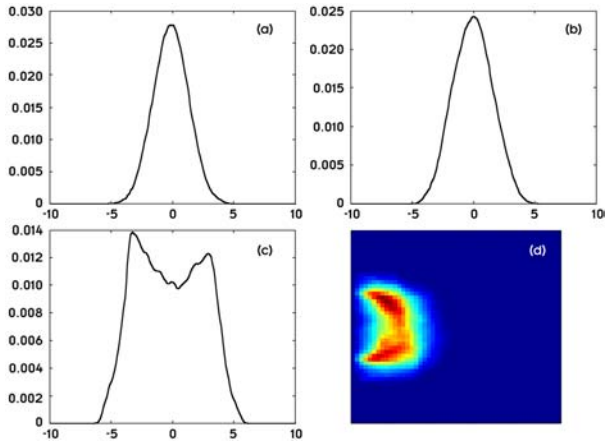

Fig. 2. Examples of projected mass measurements for spindle of Fig. 1. Horizontal axes for (a)–(c) are in microns; vertical axes represent the fraction of total mass. (a) Mass projected onto first principal axis. (b) Mass projected onto second principal axis. (c) Mass projected onto third principal axis. (d) Mass projected onto planes parallel to first and second principal axes at intervals along third principal axis. The vertical axis represents location along the third principal axis in microns, where zero is the center of mass and the horizontal axis represents radial distance, in microns, from the third principal axis. The color scale represents fraction of total mass.

38. Skewness of left half of the mass projected onto the third principal axis.
39. Kurtosis of left half of the mass projected onto the third principal axis.
40. Skewness of right half of the mass projected onto the third principal axis.
41. Kurtosis of right half of the mass projected onto the third principal axis.
42–5. Radial mass percentiles of mass projected onto plane of first and second principal axes. These are radial intervals (in microns) in the plane of the first and second principal axes which contain 25%, 50%, 75%, and 95% of the total spindle mass, respectively.
46–49. Principal component coefficients of mass projected onto planes parallel to the plane of the first and second principal axes. We select 50 equally spaced intervals along the third principal axis ranging from –10 to +10 μm from the center of mass. In each of these intervals, we compute the fraction of total mass in 50 equally spaced radial intervals from 0 to +10 μm from the third principal axis. The result is a 50 × 50 2D array that is a function of radius (in the plane) and distance from center of mass along the third principal axis. An example of this projected mass is shown as an image in Fig. 2(d). Note the two peaks which again correspond to the spindle poles. We perform principal components analysis on this on the 2500-point vectors obtain by raster scanning the 50 × 50 array and keep only the first four coefficients.

Software was developed in the MATLAB environment to automatically extract all of the above features from the image stacks.

Results and Accomplishments

The 49 features described above were computed for each of the 40 spindles that were imaged. The values of these features were then compared for different pairs of data sets using one-way analysis of variance (ANOVA). The p-values from these ANOVA tests are given in Table 1.

Analyzing the first data column of Table 1, we note that for the WT-vs-p53-KO comparison there are 27 features that are different at $p < 0.03$. As we would expect to see only about one or two features different at $p < 0.03$ (since $0.03 \times 49 = 1.47$), this is a clear indication that the WT and p53-KO spindles are significantly different with respect to the computed features. In the second data column, we compare p53-KO to p53-KO-TaxLo. Here we see that there are 13 features that vary at $p < 0.03$. Again, the features indicate a quantifiable difference in the spindles. In the third data column of Table 1, we compare the p53-KO-TaxLo to p53-KO-TaxHi. Only one feature is different at $p < 0.03$, and since we might expect one or two features at $p < 0.03$ purely by random chance, this indicates that there are essentially no quantifiable differences between these two sets with respect to the features computed. This indicates that both the high and low concentrations of Taxol induce quite similar effects in the spindles. In the final data column, we compare WT to the VPARP-KO cells. In this case, we find five features that differ at $p < 0.03$. This evidence indicates that the wild-type and VPARP-knockout spindles do indeed exhibit differences, but there are fewer such differences in this case than WT-vs-p53-KO case.

Summary and Conclusions

We recall, as stated in the abstract, that the two primary objectives of this project were (1) to construct a database of mitotic spindle imagery from wild-type and knockout (mutant) mouse cells and (2) to develop proof-of-concept, automated image analysis tools to characterize and compare the observed structures. As evident from the previous sections, we have successfully achieved both of these primary objectives. Furthermore, the results of the analysis have demonstrated that both p53-KO and VPARP-KO spindles exhibit quantifiable differences from WT spindles. These results were obtained via software and algorithms developed to perform automated analysis of 3D confocal microscopy images. Since the mitotic spindle is a crucial structure in cell-cycle progression, and since

Table 1. Collection of p-values from one-way ANOVA
Features different at p <0.03 are shaded

Feature	WT vs. p53-KO	p53-KO vs. p53-KO-TaxLo	p53-KO-TaxLo vs. p53-KO-TaxHi	WT vs. VPARP-KO
1	0.001100	0.216930	0.742420	0.000967
2	0.016648	0.125270	0.497540	0.001426
3	0.000008	0.167500	0.171880	0.172870
4	0.000102	0.122130	0.183460	0.672430
5	0.020666	0.000016	0.023851	0.599550
6	0.014652	0.499240	0.968500	0.001207
7	0.830570	0.554860	0.092413	0.231380
8	0.830030	0.540580	0.902870	0.295980
9	0.015389	1.000000	0.794190	0.790010
10	0.002535	0.900400	1.000000	0.798600
11	0.006921	0.769620	0.953030	0.435070
12	0.020876	0.613750	1.000000	0.099915
13	0.005776	0.468370	0.896140	0.456690
14	0.011732	0.261670	0.908000	0.118680
15	0.227180	0.825320	0.378690	0.513280
16	0.263140	0.439310	0.102700	0.149360
17	0.057692	0.060344	0.423860	0.778920
18	0.508910	0.077402	0.912250	0.011427
19	0.485960	0.644610	0.770330	0.316980
20	0.730720	0.415440	0.174470	0.350070
21	0.249250	0.748570	0.289560	0.629520
22	0.009242	0.147420	0.836600	0.950480
23	0.801310	0.230810	0.197920	0.475720
24	0.000016	0.094417	0.748320	0.316810
25	0.635920	0.813610	0.964130	0.605840
26	0.865520	0.705520	0.407840	0.939310
27	0.339630	0.577150	0.430680	0.945780
28	0.000715	0.000318	0.098707	0.020092
29	0.000040	0.007702	0.391660	0.781440
30	0.000008	0.003143	0.243640	0.825680
31	0.000014	0.003072	0.519390	0.866930
32	0.000159	0.002471	0.859190	0.798970
33	0.000001	0.002628	0.421900	0.885090
34	0.870750	0.021608	0.724500	0.945770
35	0.084633	0.028553	0.571950	0.988380
36	0.271430	0.052767	0.521250	0.149250
37	0.000370	0.663360	0.218600	0.089845
38	0.002539	0.045054	0.171260	0.134810
39	0.001925	0.061579	0.144530	0.128000
40	0.000015	0.000283	0.971010	0.871750
41	0.000012	0.000322	0.981600	0.864620
42	0.071363	0.549460	0.659140	0.948180
43	0.287360	0.852210	0.607640	0.790310
44	0.938410	0.906100	0.621420	0.677790
45	0.163670	0.131070	0.824360	0.348410
46	0.000017	0.009114	0.310020	0.962760
47	0.008446	0.418190	0.682500	0.679810
48	0.146150	0.016600	0.530830	0.969500
49	0.641360	0.206300	0.044541	0.707530

there are multiple proteins that interact with the spindle in unknown ways, the developed software and algorithms will be broadly applicable in investigating the effects of other associated proteins on spindle morphology. Understanding the interactions of such proteins with the spindle may uncover future anti-cancer drug targets.

This project has demonstrated proof-of-concept for the application of automated image analysis to enable high-throughput analysis of mitotic spindle imagery. The next phase of this work is to apply the developed techniques to the analysis of living cells. The mitotic spindle is a dynamic structure that we have currently only examined in a fixed state. It is likely that more—and perhaps quantitatively more pronounced—differences between wild-type, knockout, and/or drug-treated cells will be observed as we examine the spindle dynamics through its formation and function in living cells. The analysis spindles in living cells will be the focus of follow-on efforts we are currently pursuing with the National Institutes of Health. Specifically, we are currently preparing a multi-year proposal to be submitted to the "Innovations in Biomedical Computational Science and Technology" program (PAR-03-106) in February 2004. We believe that the successful preliminary results obtained and the proof-of-concept established with this project will enable us to make a strong proposal.

References

[1]K. Fukasawa, T. Choi, R. Huriyama, S. Rulong, and G. F. Vande Woude, "Abnormal Centrosome Amplification in the Absence of p53," *Science* **271**, 1744 (1996).

[2]J. Foote and A. Raman, "A relation between the principal axes of inertia and ligand binding," in *Proc. of the National Academy of Sciences* **97**, 978 (2000).

[3]K. Fukunaga, *Statistical Pattern Recognition*, 2nd Ed., Morgan Kaufmann, 1990.

Ontology-Based Three-Dimensional Modeling for Human Anatomy

L. C. Pouchard and S. P. Dickson
Computer Science and Mathematics

The project focused on the problem of seamlessly presenting a human anatomical three-dimensional (3D) model with other types of systemic information ranging from physiological to molecular information while navigating the anatomical model. We proposed solutions that include a visual 3D interface with navigation features that integrate structured information display and the adaptation of an ontology of medical information where several types of indicators are formally and semantically linked. The anatomy serves as a visual entry point to medical indicators and other information about a patient. The ontology of medical information provides labeling to the highlighted anatomy parts in the 3D display. Because of the formal structure and links between anatomical concepts found in the ontology, the navigation is greatly enhanced: navigation based on both 3D visual images and text and formal links representing anatomical concepts within the model becomes possible.

Introduction

As the use of computer modeling spreads in medical research, smarter models of the human anatomy are needed in a broad range of applications, including clinical diagnosis, surgical planning,[1] cancer treatment using radiation therapy,[2] and other applications. In silico models constructed in computerized simulation are used to determine the effects of parameter variations and compare between actual clinical data and simulation results. Static models of human anatomy in two-dimensional (2D) slices from 3D geometric coordinates are now available to clinicians and researchers for visualization, diagnosis, measurements and other purposes. From scans such as X-ray Computed Tomography (CT) or magnetic resonance imagery (MRI) volumetric reconstructions of the human body are created. However, the volumetric reconstructions have not been used for 3D animations for scientific and medical purposes, in part to due to computational complexity and resource requirements.

In addition, researchers, clinicians, and practitioners who analyze computerized segments of the anatomy do not have the ability to integrate different types of medical data. There is also a lack of easy-to-use capabilities to facilitate analysis and increase accuracy. At the time of data analysis and visualization, scientists must rely on their own mental models to integrate into a coherent whole information provided by different systems and represented in several media: multiresolution imaging, property measurements (physiological, mechanical, etc.), standardized annotations of anatomy, characterized links between parts of the anatomy, sensor data, and others.

Faced with an explosion of parameters to consider when making decisions, researchers and practitioners need new computerized environments where various media types and tools are seamlessly integrated and easily manipulated at the point of service.[3] Tools for analysis and diagnosis guidance may be critical for the quick assessment of an emergency situation. This is particularly true when split-second assessment of an injury is required, for instance by paramedics in the field of battle.[4]

Based on this research, a proposal to the DARPA Virtual Soldier Program (VSP) Phase I[5] was submitted and selected to participate under sponsorship of the United States Army Medical Research and Materiel Command (USAMRMC) (DOE Proposal Number 1868-HH48-X1). Whereas results described below were innovative and proved highly applicable to the work in the VSP, the scope of the analysis was restricted by effort and resources.

Technical Approach

Animated human models have been developed in the cinematic industry with an emphasis on good appearance rather than accuracy of representation. The level of detail and accuracy of 3D models appropriate for the needs of scientific representation has been one of two research directions investigated in this project. It included accurately and precisely identifying anatomical parts with 3D volumetric coordinates at a level of precision not achieved previously, visualizing parts of the anatomy with this new level, and easy-to-use adding navigation capabilities. The foot was chosen for visualization as an example of an anatomical part for its concentration of interacting small muscles and bones, and variety of tissue (Fig. 1). The chosen development environment for 3D animation is Maya™,[6] a highly flexible environment with solid community support and numerous extensions.

Fig. 1. Foot volumetric data.

A multilevel information infrastructure was also investigated. This infrastructure permits associating each modeled part of the anatomy and its corresponding geometric coordinates to a web of textual information and properties contained in an ontology. An ontology is a declarative, symbolic model that formalizes (anatomical) concepts, terminology, and abstract relationships between these concepts and axioms or logical rules on how relationships inform concepts. All items in an ontology are called frames. An ontology is best imagined as a web of information structured with links and semantic definitions. The information may include text, parts of speech, concepts, images, or mathematical coordinates that are linked with each other by logical relationships described in rules. It is by design human and machine-readable, nonexhaustive, and able to accommodate new types of information and concepts thanks to its formal specifications when discoveries are being made. Some purposes of ontologies include creating standards on a particular topic, declare machine-readable specifications, and re-use of components. The Digital Anatomist Foundational Model (FMA) is the domain ontology we used to accommodate the needs of the future sponsor.

The FMA is developed at the University of Washington and contains approximately 100,000 terms representing 70,000 concepts, 120 logical relationships iterated over a million times between the terms.[7] As an example, in the FMA, tissues are related to each other through abstract relationships such as "has boundary," "is a tributary of," "is contiguous to," and many others. The FMA is based on the *Terminologia Anatomica*. In addition, it also includes physiological and some cell-related information that is characterized with relationships to anatomical entities.

The approach also included search and retrieval mechanisms that were both appropriate to the visualization environment and would return accurate and meaningful answers for the scientist. As a simple mouse-over within the visualization by the user translates into a computerized query to the FMA, the depth of ontological navigation was taken into account and set. Query and return formats to the visual interface were also investigated because the format of a query and its display affect the number of nodes traversed in the ontology.

Results and Accomplishments

The results found here are based on heuristics and the researchers' experience, and do not include metrics. They are still valuable because they guide the choice of computer architecture for integrating visual, textual, and logical information. This research proved necessary for developing a middleware architecture for the Virtual Soldier Program and of is expected to continue under the USARMC sponsorship.

Testing Search Mechanisms

The FMA is available through a web interface that uses the Foundational Model Explorer (FME).[8] A text string such as "metatarsal bone" in the query box and a check on the sub-class for the type of query returns all the information available on this anatomical part contained in the FME. Figure 2 shows the results of a query for the metatarsal bone as a subclass of bone in the FME. The relationships show that "metatarsal bone" is part of the foot, has itself three parts, has a boundary, an inherent 3D shape, and no synonym. (By contrast, blood as an anatomical part has a definition, synonyms, a boundary, but no 3D shape). Figure 3 shows the web of concepts that constitute the results of a query for the talus as part of the foot. But the heel of the foot is a subclass of foot with a synonym of heel region and calcaneal region. This

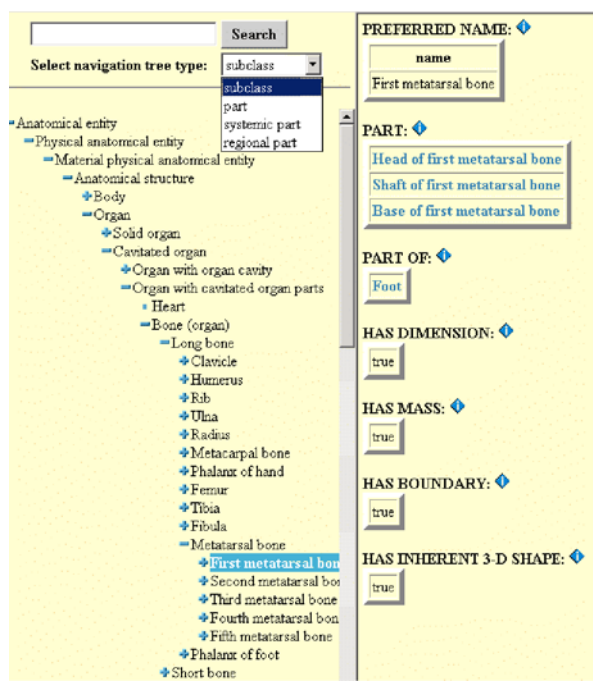

Fig. 2. First metatarsal bone in the FMA.

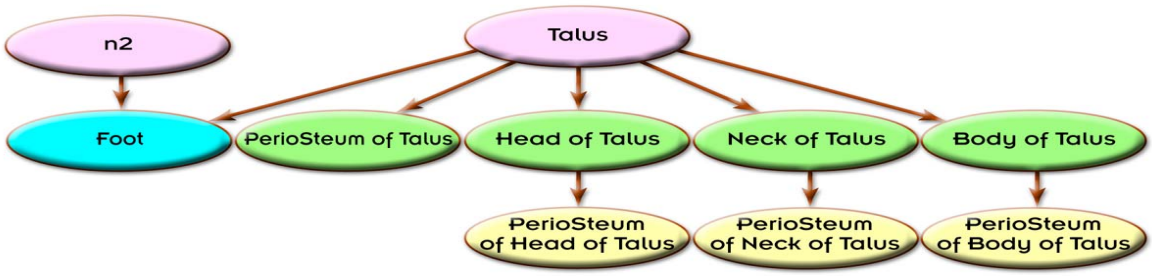

Fig. 3. Some nodes and edges in the talus as part of the foot.

example illustrates the complexity of relationships in an anatomical description of what is commonly thought of as a part of the body. The FMA is mostly used for educational purposes at present, but our part of research illustrates other usages such as use in diagnosis when it is integrated to a visual environment.

The choice of a computer architecture that would enable searches to the ontology by mouse-over 3D modeling (i.e., the integration between the ontology and the visualization environment) was guided by search mechanisms. Searches in an ontology are more complex than searches in a database because ontologies allow more general query formulations and more precise definitions at the same time (and thus are more flexible). The strength of an ontology comes from the possibility to do searches using rules rather than string matches as in a relational or object-oriented database. As exemplified above for the FMA, a search on a string can be specified as "string as part of" or "string as subclass" or "string as relationship" where relationship is any of the relationships contained in the FMA. Two caveats to point out are the complexity of queries to construct and the necessity to know the relationships included in the ontology of choice. However, this last caveat is also valid for any database search and well documented in the literature of information retrieval.

A search in an ontology can represent a large number of queries to a database. Query language and formats for the returned answers were considered as they dictated the choice of architecture for integrating with visualization and accuracy of representation. We tested the Ontology Querying Agent for the Foundational Model of Anatomy (OQAFMA) query language developed with the FMA,[9] and the Protégé query mechanisms[10] for suitability to a visualization environment.

Analysis and Discussion of Search Mechanisms

OQAFMA is based on STRUQL, a modified version of SQL to include rule-based searches. For a given query, OQAFMA traverses the entire tree of the FMA, and returned results are guaranteed to bring closure to a search. This means that nodes satisfying the criteria are returned, not only at the first level of the FMA tree where strings are found, but also at all branches of the tree down to the last leaf satisfying the criteria. This is called bringing closure in a search. By contrast, a search using Protégé search mechanisms does not bring closure as it returns only the first level of nodes in the tree. To obtain closure, parsing each return to a search and sending new searches based on relationships found between returned frames until a search returns no result is necessary with Protégé. While OQAFMA appears a more economical and elegant solution, its returns are formatted as an XML document. Because XML cannot easily represent a tree hierarchy and a web of relationships and rules for combining frames (due to its ancestry), OQAFMA results are not suitable for use in a visualization environment without further adaptation. In addition an OQAFMA query must be constructed in the Knowledge Interchange Language.[11]

Example: Search for talus using OQAFMA.
Query:

```
Where
X->":NAME"->"talus",
X->"part"+->Y,
Y->":NAME"->Parts
CREATE
TheTalus(Parts)
```

A good knowledge of KIF is required to formulate the query corresponding to a search in OQAFMA. Due to the million + iterations (i.e., meaningful combinations) possible with the frames in the FMA, searches must be reduced by the developers of the tool. A good rule of thumb is to reduce the number of queries according the level of detail in the visualization.

Results:

```
<results>
  <Talus>
    <Parts>Head of talus</Parts>
  </Talus>
  <Talus>
    <Parts>Neck of talus</Parts>
  </Talus>
  <Talus>
    <Parts>Body of talus</Parts>
  </Talus>
.....
```

```
<Talus>
  <Parts>Periosteum of head of talus</Parts>
 </Talus>
 <Talus>
  <Parts>Periosteum of neck of talus</Parts>
 </Talus>
 <Talus>
  <Parts>Periosteum of body of talus</Parts>
 </Talus>
…..
<results>
```

As is clearly visible here when contrasted with Fig. 3, Periosteum of head, neck, and body of talus are treated as equal elements in an XML representation, and the tree hierarchy exemplified in Fig. 3 has disappeared.

Visualization

Architecture: The system is prototyped as a collection of Maya plugins.

DH_selectEntity is declared in Maya as a global procedure which is called when the user selects an entity from the Digital Human customized Marking Menu. DH_selectEntity maps from the Foundational Model of Anatomy (FMA/Protege) entity name to the name of the corresponding geometry node in the Maya scene graph (DAG) then selects the appropriate geometry node for focus.

Global procedure DH_selectionChange is a custom Maya Embedded Language (MEL) command executed upon a change of the selection list. DH_selectionChange maps from the selected geometrical entity in the Maya Scene Graph (DAG) to the corresponding ontological name for the node. DH_selectionChange builds and sends the query to the Foundational Model of Anatomy (Protégé server) and collects the results. DH_selectionChange then edits the marking menu to reflect the relational information relevant to the current focus context.

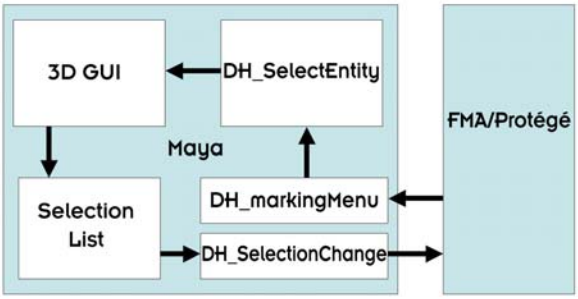

Fig. 4. Maya plugin architecture.

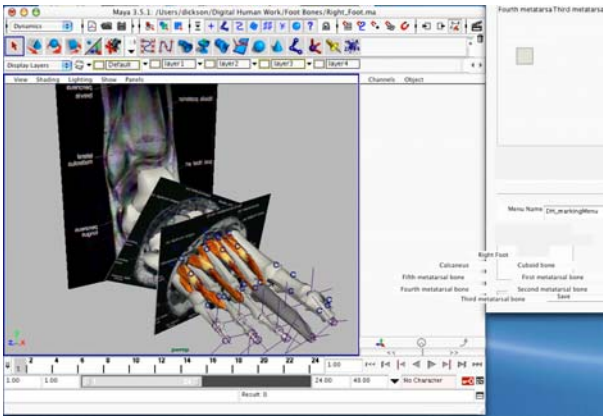

Fig. 5. Knowledge-guided 3-D user interface.

Summary and Conclusions

The FMA and its various access interfaces was obtained from the University of Washington (UW) and resides on an ORNL server. Collaboration with UW has been developed for maintenance at ORNL, and for purposes as needed in the VSP. At this time, ORNL is not expected to become a mirror site. Access to the FMA data and ORNL visualization architecture from team members of the VSP is already being planned within the framework of DOE proposal 1868-HH48-X1. Search mechanisms have been tested for seamless access by computer applications and re-usable Maya and Protégé API modules have been developed. Searches have been integrated to a 3D visualization environment for navigation.

Further research directions have been open for access to ontology architectures, ontology searching languages, and visualization that will be explored in the VSP. In particular, the need for metrics for ontology searches and level of detail in visualization have been highlighted.

References

[1]J. D. Westwood et al., editors, *Medicine Meets Virtual Reality 2000*, IOS Press, Amsterdam (2000).

[2]F. M. Kahn, *The Physics of Radiation Therapy*, 2nd Ed., Williams & Wilkins, Baltimore (1994).

[3]R. M. Satava, "Cybersurgeon: Advanced simulation technologies for surgical education," *Medical Simulation and Training* **1**, 6–9 (1996).

[4]R. M. Satava, "Medical Virtual Reality,"pp. 100–105 in *Medicine Meets Virtual Reality: 4 Health Care in the Information Age – Future Tools for Transforming Medicine,* IOS Press, Amsterdam.

[5]The Virtual Soldier Program. http://www.virtualsoldier.net.

[6]The Maya Family. ©2000–2003 Alias Systems, a division of Silicon Graphics Limited. All rights reserved.

[7]C. Rosse, L. G. Shapiro, and J. F. Brinkley, "The Digital Anatomist Foundation Model: Principles for Defining and Structuring its Concept Domain," *J Am Med Inform Assoc*. American Medical Informatics Association (AMIA) 1998 Symp. Suppl. 1998:820–824. http://sig.biostr.washington.edu/projects/fm/index.html.

[8]FME, http://sig.biostr.washington.edu/projects/fm/FME/index.html.

[9]OQAFMA. Forthcoming paper by Peter Mork. http://quad.biostr.washington.edu/noqafma/index.html.

[10]Protégé 2000, http://protege.stanford.edu/.

[11]M. Genesereth and R. E. Fikes, *Knowledge Interchange Format*, Version 3.0. Reference Manual, Technical Report Logic-92-1. Computer Science Department, Stanford University, Stanford, California, January 1992.

The Global Optimization Problem for Remote Sensing: A Guaranteed, Efficient Solution

J. C. Wells, V. A. Protopopescu, and C. D'Helon
Computer Science and Mathematics Division

We establish proof of principle that a broad class of continuous global-optimization problems (GOPs) can be solved efficiently, with a guarantee, by exploiting available additional information in the problem. We demonstrate that our proposed algorithm is considerably more efficient than current algorithms and apply our methodology to a remote sensing problem in the atmosphere, namely, monocular passive ranging (MPR). The expected deliverable will be a robust, efficient, and validated software tool, which will be useful in solving GOPs efficiently, where the need for the optimal—as opposed to a suboptimal—solution is critical.

Objective

Independent of specific approach and algorithmic efficiency, current solutions for continuous GOPs,[1] share a common drawback in that none of them can guarantee that the global minimum will be found in a reasonable time.

We aim to develop a new algorithm that can efficiently solve the continuous GOP arising from monocular passive ranging[2] and guarantee the result. MPR determines the instantaneous range to a target relying on remote sensing in the atmosphere, using a single sensor. Our choice of application is motivated by yet unsolved challenges facing the Department of Defense Missile Defense Agency (MDA), instances of which require the optimal, as opposed to a suboptimal, solution of a GOP.

Our new algorithm guarantees to find the global minimum by systematically using additional information about the error function between the predicted and observed radiances in MPR. This information may include the size of the basin of attraction for the global minimum, the separation between the global minimum and the next lowest local minimum, the general shape of the error function, and the uncertainties inherent in the sensor measurements. Indeed, some degree of information is usually available in many applications, but present algorithms either do not or cannot use it. This new idea enables us to map the continuous GOP onto a discrete search, by eliminating all basins of attraction except that of the global minimum.

The performance of our approach can be assessed in terms of a set of benchmark objective functions to show that the new algorithm is more efficient than present algorithms, as well as in terms of how much additional information is sufficient to guarantee that the global minimum is found quickly and accurately, for the error function in MPR.

By the end of October, we successfully implemented our algorithm to solve continuous GOPs. An authoritative benchmark for calculating atmospheric radiation transmission, MODTRAN,[3] was used to generate the error function between the predicted and observed radiances in MPR. Multiple minima in the error function were observed for fluctuating ozone profiles, since the ozone density is non-monotonic as the altitude increases. The algorithm was also parallelized on the IBM Power 4 supercomputer within ORNL's Center for Computational Sciences, in order to address independent fluctuations in multiple ozone layers, and thus expand the dimensionality of the error function.

Varying degrees of additional information about the error function were assumed in order to investigate how much information is required to eliminate all basins of attraction except that of the global minimum. Our results to date (for up to four dimensions) indicate that the error function available in MPR is likely to contain sufficient additional information to guarantee that the global minimum is found in a reasonable time. We have investigated the time scaling of the new algorithm, as well as the probability of finding the global minimum, and found that information related to the size of the basin of attraction for the global minimum is of prime importance for an efficient guarantee.

We have compared the performance of our algorithm with that of the TRUST algorithm[4] for a set of seven standard benchmark functions. The results show that our approach has the ability to outperform TRUST, in terms of the number of function evaluations, at least for two-dimensional objective functions. As the number of dimensions grows, our algorithm requires an exponential increase in the number of function evaluations. We have yet to investigate the possibility that our algorithm can

outperform TRUST for high-dimensional problems, in the case that the global minimum has a relatively narrow basin of attraction. In any case, our approach guarantees that the global minimum will be found, something that TRUST cannot achieve in principle. Thus, in general, a completely conclusive comparison between the two algorithms is impossible.

Our algorithm is applicable to a broad class of continuous GOPs, arising in a wide range of applications that are relevant to strategic ORNL thrusts in national security, materials science, and computational biology. Many of the problems in these areas require precise, guaranteed identification of the global minimum and will benefit from this research.

There is also an immediate need and opportunity to apply our algorithm to the challenges facing national defense. Remote sensing in the atmosphere is currently a critical field of research within strategic and theater missile defense. Monocular passive ranging is a prime example of a problem that will benefit from our optimal GOP solution for accurate ranging, with a guarantee.

References

[1]R. Horst and H. Tuy, *Global Optimization*, 2ed., Springer-Verlag, Berlin, 1993.

[2]W. Jeffrey, J. S. Draper, and R. Gobel, "Monocular Passive Ranging," *IRIS Targets, Backgrounds and Discrimination Conference*, 1994.

[3]MODTRAN website: http://www-vsbm.plh.af.mil/soft/modtran.html.

[4]J. Barhen, V. Protopopescu, and D. Reister, "TRUST: A Deterministic Algorithm for Global Optimization," *Science* **276**, 1094 (1997).